AGU100 ADVANCING EARTH AND SPACE SCIENCE

JGR Atmospheres

RESEARCH ARTICLE
10.1029/2018JD028673

Key Points:
- The GW activity derived from 302 nights of lidar measurements above a subpolar region and from collocated satellite measurements is evaluated
- The GW specific potential energy from lidar and satellite measurements is larger inside the polar vortex than outside it or at its edge
- The specific potential energy is larger during winter and spring

Correspondence to:
P. Llamedo,
pllamedo@austral.edu.ar

Citation:
Llamedo, P., Salvador, J., de la Torre, A., Quiroga, J., Alexander, P., Hierro, R., et al. (2019). 11 years of Rayleigh lidar observations of gravity wave activity above the southern tip of South America. *Journal of Geophysical Research: Atmospheres*, *124*, 451–467. https://doi.org/10.1029/2018JD028673

Received 21 MAR 2018
Accepted 12 DEC 2018
Accepted article online 17 DEC 2018
Published online 17 JAN 2019

Author Contributions:
Conceptualization: P. Llamedo, A. de la Torre, J. Quiroga
Data curation: P. Llamedo, J. Salvador, J. Quiroga, R. Hierro, T. Schmidt, A. Pazmiño, E. Quel
Formal analysis: P. Llamedo, J. Salvador, J. Quiroga, A. Pazmiño
Funding acquisition: A. de la Torre, J. Quiroga, T. Schmidt, A. Pazmiño
Investigation: P. Llamedo, J. Salvador, A. de la Torre, P. Alexander, R. Hierro
Methodology: P. Llamedo, J. Salvador, A. de la Torre, J. Quiroga, P. Alexander, R. Hierro
Supervision: A. de la Torre, J. Quiroga
Validation: P. Llamedo, J. Salvador, A. de la Torre, P. Alexander
Visualization: P. Llamedo
Writing - original draft: P. Llamedo
Writing – review & editing: P. Llamedo, J. Salvador, A. de la Torre, J. Quiroga, P. Alexander, R. Hierro, T. Schmidt, A. Pazmiño, E. Quel

11 Years of Rayleigh Lidar Observations of Gravity Wave Activity Above the Southern Tip of South America

P. Llamedo[1], J. Salvador[2,3,4], A. de la Torre[1], J. Quiroga[2,4], P. Alexander[5], R. Hierro[1], T. Schmidt[6], A. Pazmiño[7], and E. Quel[3]

[1]LIDTUA, CIC, Facultad de Ingeniería, Universidad Austral and CONICET, Buenos Aires, Argentina, [2]Laser and Application Research Center (CEILAP)–UNIDEF (MINDEF-CONICET), Villa Martelli, Argentina, [3]Facultad Regional Buenos Aires (UTN-FRBA), Universidad Tecnológica Nacional, Buenos Aires, Argentina, [4]Universidad Nacional de la Patagonia Austral, Unidad Académica Río Gallegos, and CIT, Río Gallegos, Argentina, [5]Instituto de Física de Buenos Aires, CONICET, Buenos Aires, Argentina, [6]Helmholtz Centre Potsdam, GFZ German Research Centre for Geosciences, Potsdam, Germany, [7]LATMOS, UVSQ University Paris Saclay, UPMC University Paris 06, CNRS, Guyancourt, France

Abstract Gravity wave (GW) activity is analyzed using temperature (*T*) data retrieved from a Rayleigh light detection and ranging (lidar) at Río Gallegos, Argentina (51.6°S, 69.3°W). GW characteristics are derived from 302 nights of observations providing more than 1,018 hr of high-resolution lidar data between 20- and 56-km height from August 2005 to December 2015. *T* measurements are performed by a Differential Absorption Lidar instrument. This lidar was the southernmost outside Antarctica until the end of 2017. Río Gallegos is an exceptional place to observe large amplitude GW. Every lidar measurement is classified according to its relative position to the polar vortex. The lidar measurements are compared with collocated Sounding of the Atmosphere using Broadband Emission Radiometry and Global Positioning System-Radio Occultation data. The different instruments show different windows of the GW spectrum, providing complementary observations. In general, the geometric mean of the specific GW potential energy (*PE*) is larger during winter and spring than during summer and autumn. The largest geometric mean of *PE* is found inside the vortex and decreases monotonically at its edge, outside it and when there is no vortex. The same behavior is observed with satellite data. On average, it can be seen that lidar observations provide larger *PE* values than limb sounding measurements. From a Morlet continuous wavelet transform analysis, three distinct modes are captured from Sounding of the Atmosphere using Broadband Emission Radiometry and from Global Positioning System-Radio Occultation data at the upper and lower stratosphere, respectively. In particular, a systematic 3.5- to 4-year oscillation, possibly related to El Niño–Southern Oscillation is observed.

1. Introduction

The role of gravity waves (GWs) in the forcing of global-scale circulation and in the thermal structure of the lower and middle atmosphere has been largely recognized (e.g., Nappo, 2002). The main sources of GW in the lower and middle atmospheres are deep convection, topographic forcing, shear generation, geostrophic adjustment, and wave-wave interaction. GWs transfer energy and momentum from their sources in lower layers of the atmosphere to levels where they dissipate in the stratosphere and mesosphere (Fritts & Alexander, 2003). Depending on the horizontal wind shear, GW may be also refracted or dissipated, a process known as critical-level filtering.

More than one decade of global satellite observations in the troposphere-stratosphere has shown that during winter and spring, the leeward of the southern Andes mountains region exhibits some of the largest GW amplitudes, energy densities, and momentum fluxes (MFs, e.g., de la Torre et al., 2012; Hindley et al., 2015; Hoffmann et al., 2016, 2013; Sato et al., 2012). General circulation models (GCMs) cannot resolve subgrid-scale effects like GW drag and diffusion processes, which must be included via parameterizations. In general, during the southern wintertime polar vortex breakdown, winds and temperatures are not well reproduced by GCM. This feature may be due to deficient model parameterizations of GW drag in the stratosphere near 60°S (McLandress et al., 2012). Thus, the availability of accurate high-resolution measurements of GW parameters in this area is of major relevance.

The southern tip of South America is the southernmost landmass to the north of the Antarctic Peninsula. During the Southern Hemisphere spring (September to November) the polar vortex weakens and its edge advances northward, sometimes beyond Río Gallegos. The vortex edge constitutes a dynamical barrier that separates air masses, resulting in a locally enhanced T gradient. It is known that in the vicinity of the polar vortex, spontaneous adjustment processes around the stratospheric jet generate large amplitude GW (e.g., Plougonven & Zhang, 2014). The westerly prevailing flow over the southern part of the Andes range represents the second main source of GW. These waves may be enhanced in the presence of the jet, avoiding possible critical level filtering. P. Alexander et al. (2010) analyzed GW activity in the lower stratosphere over the southernmost Andes Mountains and their prolongation in the Antarctic Peninsula by Global Positioning System (GPS) radio occultation (RO) temperature profiles, between years 2002 and 2005 via the CHAllenging Minisatellite Payload (CHAMP) mission. They found a significant seasonal variation of wave activity and the locations of significant cases indicate that topography is an important source. Some strong wave activity is also found over the open ocean. Critical level filtering was shown to have an attenuation effect, implying that a large fraction of the observed activity can be considered to be an outcome of mountain waves (MWs). The region mostly generates wave fronts closely aligned with the north-south direction (almost parallel to the mountains), whereby this geometry favors wave detection by the nearly meridional line of sight characterizing most of the GPS RO observations used.

Sato et al. (2012), using a high-resolution GCM, found large GW enhancements in winter leeward of the southern Andes, the Antarctic Peninsula, and in the region surrounding the polar vortex in the middle and upper stratosphere, while the GW energy is generally weaker in summer. Baumgaertner and McDonald (2007) attributed the enhancements around the edge of the polar vortex to reduced critical level filtering and Doppler shifting. GW generated at the southern Andes can be refracted poleward by the vortex jet. Ehard et al. (2017) analyzed a large amplitude mountain wave above New Zealand that was refracted southward due to the strong meridional shear. Pulido et al. (2012) suggested that high GW activity found by several studies over Drake Passage may have an orographic origin at the Andes. A similar result was found by Jiang et al. (2013), who reported that GW originated at the Patagonian Andes propagates poleward and that the lateral shear of the horizontal wind along the edge of the polar vortex plays a constructive role in the poleward momentum transfer. Plougonven et al. (2013), from mesoscale simulations and stratospheric balloons from the Vorcore campaign, provided a comparative description of the GW field in the lower stratosphere above Antarctica and the Southern Ocean during the austral spring of 2005. They reported a different behavior between orographic (overestimation in the simulations relative to the observations) and nonorographic GW (underestimation). These authors remarked the need to distinguish and quantify orographic and nonorographic sources. A comparison between GW MF in models and those derived from observations over large geographical areas was performed by Geller et al. (2013). Measurements generally showed similar MF magnitudes as in models, except that the MF derived from satellite measurements falls off faster with height. A comparison was performed during October 2005 over Antarctica, and enhanced MF over the region and/or southern Andes topography was observed. Preusse et al. (2014), using Global model data obtained from the European Centre for Medium-Range Weather Forecasts (ECMWF), identified orographic and nonorographic sources.

Diverse sources of high GW variance were proposed at this region: fronts (Richter et al., 2010), convection (Choi & Chun, 2013), small islands (Hoffmann et al., 2013), and large eddy growth instabilities at 500 hPa in the storm tracks (Hendricks et al., 2014). Hindley et al. (2015) from GPS RO data from the Constellation Observing System for Meteorology, Ionosphere, and Climate (COSMIC) satellite constellation determined the properties of GW in the hot spot and beyond. S. P. Alexander et al. (2016) analyzed the spatial and temporal variability of total MF and intermittency in the Southern Hemisphere extratropics using the free-running Kanto model, which does not have any GW parameterization. They found results consistent with absolute MF determined from satellite limb and superpressure balloon observations. Reinforcing the relative importance of orographic against other sources, Wright et al. (2017) developed a spectral analysis method for detecting and characterizing GW using a 3-D S-transform and AIRS satellite data. The southern Andes and Drake Passage were considered. Their method allows to characterize GW across the full range of length scales present in the input data. They observed that the MF in this region is primarily directed directly upwind and is greatest above mountainous regions, consistent with previous studies.

The lidar (light detection and ranging) technique is a powerful tool to study GW activity in the upper stratosphere/lower mesosphere with high temporal and vertical resolution. Lidar data were used to study the GW-induced stratospheric warming and the GW-stratospheric vortex interaction in the Northern Hemisphere (e.g., Duck et al., 1998). Duck et al. (2001) analyzed 422 nights of Rayleigh lidar observations at Eureka (80°N, 86°W) during six wintertime campaigns between 1992 and 1998. They found that GW propagating upward deposits their energy and momentum in the stratosphere, inducing a drag that reduces vortex wind speeds. In the Southern Hemisphere, most of the studies were carried out in Antarctica. For example, Kaifler, Kaifler, et al. (2015) considered 95 iron Doppler lidar observations at Davis (69°S, 78°E) between January 2011 and April 2012. They found a clear annual oscillation in GW activity showing a broad double maximum in winter. Also at Davis, Antarctica, S. P. Alexander et al. (2011) found similar results but using a Rayleigh lidar during the winters of 2007 and 2008. In the Southern Hemisphere but outside Antarctica, only a few GW studies using lidar observations can be listed. Kaifler, Lübken, et al. (2015) used Rayleigh/Raman lidar observations at Lauder, New Zealand, (45°S, 170°E) during and after the Deep Propagating Gravity Wave Experiment campaign (Fritts et al., 2016). They found that strong tropospheric winds generate large amplitude MWs that dissipate at stratospheric levels not reaching the mesosphere. Cao et al. (2016) used a narrow-band sodium lidar combined with an airglow imager at the Andes Lidar Observatory at Cerro Pachón (30.25°S, 70.73°W), Chile, to study a complex GW event on 16 January 2015 between 85- and 105-km height.

In this paper, the GW activity in terms of the *PE* using data obtained from 302 nights of lidar observations and collocated limb satellite profiles between August 2005 and December 2015 is analyzed. Sections 2 and 3 provide a description of the lidar and satellite instrument, respectively, and of the retrieval processes. Section 4 describes the data processing. Section 5 presents the wave analysis methodology, a description of wave parameters and possible filtering processes. A discussion of the observed GW variability is given in section 6, and the results are summarized in section 7.

2. Lidar Data

The Differential Absorption Lidar instrument, belonging to the Laser and Application Research Center (CEILAP, acronym in Spanish) was installed in 2005 at the Atmospheric Observatory of Southern Patagonia (OAPA, acronym in Spanish), in Río Gallegos (51.6°S, 69.3°W). This lidar was the southernmost outside Antarctica until December 2017, when a new lidar was installed in the city of Río Grande (53.5°S, 67.4°W). Roughly located at 300 km leeward of the southern Andes range and 70 km to the north of the Strait of Magellan (Figure 1), Río Gallegos is an exceptional location to observe large amplitude GW. The lidar has been operating since August 2005.

The backscattered photons are collected by four Newtonian telescopes of 0.5-m diameter each. Six digital channels record the Raman and Rayleigh backscattered photons emitted by an Excimer (XeCl) laser at 308 nm (300-mJ maximum energy) and the third harmonic of Nd-YAG laser at 355 nm (130-mJ maximum energy). Both lasers have a 30-Hz repetition rate. A simplified description of the instrument is shown in Table 1, and a detailed description can be found in Wolfram et al. (2008). Above 30-km height, T is obtained using the Rayleigh scattering technique (Hauchecorne & Chanin, 1980). Below 30-km height, the Rayleigh scattering technique is limited by aerosol scattering and ozone absorption. To overcome this problem, the inelastic Raman scattering technique is usually applied (McGee et al., 1993). However, the Raman scattering cross section is about 3 orders of magnitude smaller than the Rayleigh scattering cross section. In our system, especially designed for stratospheric ozone detection, the reception optics have been developed by means of new telescope coating. Even so, we have not been able to obtain Raman signals with reasonable signal-to-noise ratios (SNRs) at 30 km. We conclude that the Nd YAG laser should be updated or replaced by one with higher energy and also more thermally stable. The emission area is open and in contact with the external environment, which produces changes in the operating temperature of the equipment when our measurements extend throughout the night.

The corrections applied to signals involve the removal of thermal noise, sky light, and desaturation. The signal is separated into high and low sensitivity channels to increase the dynamical range. The T profile is calculated in two stages. First, the molecular density is obtained using both high and low sensitivity channels:

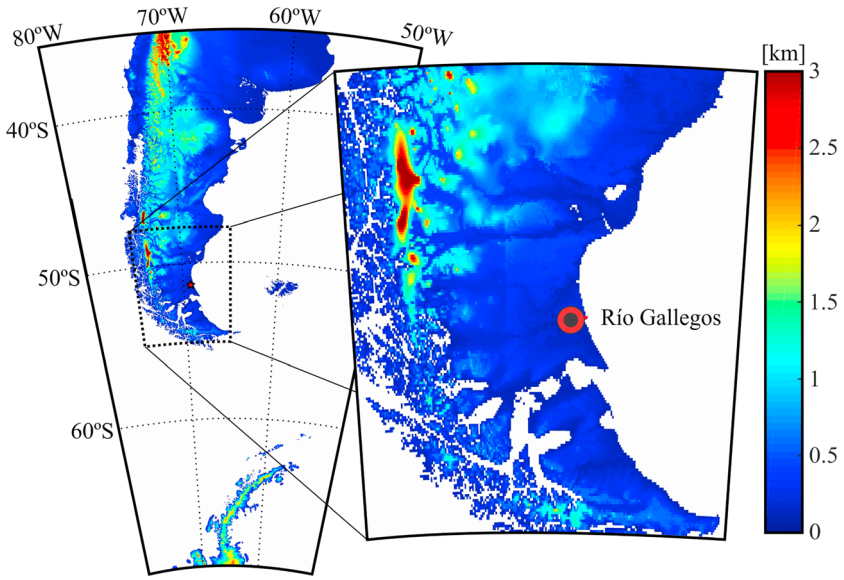

Figure 1. The topography of southern South America. The red circle indicates the location of the lidar station.

$$\rho(z) = \rho(z^*)\frac{z^2 S(z)}{z^{*2} S(z*)} q_R^2(\lambda_0, z, z^*) q_A^2(\lambda_0, z, z^*) \tag{1}$$

where z is the altitude, z^* is the density normalization altitude, $S(z)$ is the received lidar signal expressed as the number of counts in the 355-nm channel, λ_0 is the laser wavelength, q_R is the one-way molecular transmission, and q_A is the one-way aerosol transmission. q_R and q_A are given by

$$q_R^2(\lambda_0, z, z^*) = \exp\left(-2\alpha_m(\lambda_0)\int_z^{z^*}\rho\left(z'\right)\mathrm{d}z'\right) \tag{2}$$

$$q_A^2(\lambda_0, z, z^*) = \exp\left(-2\int_z^{z^*}\alpha_A\left(\lambda_0, z'\right)\mathrm{d}z'\right) \tag{3}$$

Table 1
Main Characteristics of the Raleigh Lidar System (355-nm Channel)

Subsystems		Specifications
Transmitter	Light source: Nd:YAG laser Model YG 980 manufactured by QUANTEL	30-Hz repetition rate, 130-mJ maximum pulse energy at 355 nm (third harmonic), 0.6 divergence beam, 3- to 5-ns pulse length.
Receiver	Telescopes	Newtonian configuration, diameter: 48 cm, $f/2$. Total reception area ~7,238 cm^2.
Spectrometric box	Optical fiber	HCG-M0940 T, 0.94-mm effective diameter, 0.22 ± 0.02 numerical aperture 0.2-dB/km (at 355 nm) attenuation.
	Mechanical chopper	(Before November 2009): Chopper blade, diameter 150 mm/Chopper motor: Minimotor 3564 024B, speed (min: 800, max. 9000 rpm)
		(Since November 2009): Chopper blade: Model 300 2 slot disk, diameter 102 mm Scitec Ins. Included control unit with frequency stability ±0.1% maximum frequency. Speed (min:300, max 18000 rpm)
	Diffraction grating	JOBIN-IVON I.S.A, 3,600 lines/mm with 40% transmittance at 300 nm. Dispersion 0.3 nm/mm. Spectral band width 1 nm.
Photon counting	Photomultiplier	HAMAMATSU Type H6780-03 (low sensitive at 355 nm) and HAMAMATSU Type R7400U (high sensitive), low dark current, and adapted for photon counting. Typical gain 10^6.
		(Before November 2009): Developed at Service d'Aeronomie. Six independent channels. High-speed counters of 300 MHz, 1,024-time gates/1 μs. Max count rate 40/60 count/μs.
	Acquisition	(Since November 2009):PR10-160 photon-counting system, manufactured by LICEL. Six high-speed counter 250 MHz, 16,384 bins, configured by program at 7.5-, 15-, and 150-m spatial resolution.

where $\alpha_m(\lambda_0)$ is the Rayleigh cross section and $\alpha_A(\lambda_0, z')$ is the aerosol extinction coefficient. Absorption by gases is neglected. An iterative process is performed to calculate ρ. First, an a priori ρ from the Mass Spectrometer Incoherent Scatter Atmospheric Model is used at $z^* = 30$ km, from where the contribution of stratospheric aerosols can be omitted. After an iteration in equation (1), ρ at this altitude is obtained when the relative error between two successive steps is lower than 1%. Then, a new immediately higher altitude is selected and the procedure is repeated. When the relative error of ρ between n-1 and n altitudes is less than 5%, or a SNR approaches 20, the iteration procedure is stopped. This situation typically corresponds to observations around 70-km height. Taking into account the ideal gas law and assuming that the atmosphere is in hydrostatic equilibrium, the T profile is calculated using the following approximation (Shibata et al., 1986):

$$T(z_i) = T_{\text{ref}} \frac{\rho(z_n)}{\rho(z_i)} + \frac{M}{\rho(z_i)R} \int_{z_i}^{z_n} \rho\left(z'\right) g\left(z'\right) \mathrm{d}z' \tag{4}$$

where M is the mean molecular weight of the air, g is the local acceleration of gravity, R is the ideal gas constant, and T_{ref} and $\rho\,(z_n)$ are, respectively, the reference T and the density at the top of the profile obtained from the Mass Spectrometer Incoherent Scatter Atmospheric Model.

Below 30 km, the presence of different aerosols limits the Rayleigh scattering technique. However, the lidar backscattered signal can be corrected with background aerosol to improve the accuracy. Modeled lidar signals with different loads of aerosol content reveal T values 0.5 K lower than without aerosols (Gross et al., 1997). This bias could reach 4 K due to ashes after a volcanic eruption. Aerosol backscatter coefficients are calculated from the Rayleigh lidar signal return using the Klett-Fernald algorithm (Fernald, 1984) with a reference altitude of 32 km. A quantitative knowledge of aerosol extinction to backscatter coefficient ratio is required. This ratio strongly depends on the size, shape, and refractive index of the aerosols. In the present work, a constant aerosol extinction to backscattering ratio is taken in the stratospheric altitude range and a value of 50 sr is used (Bencherif et al., 2003). The absolute air density can be derived from the backscattering signals with the lidar equation. According to this method, we first define the relative aerosol backscattering ratio as $R_{\text{aer}} = \left(1 + \frac{B_{\text{aer}}}{B_{\text{mol}}}\right)$, where B_{aer} and B_{mol} are the aerosol and molecular backscatter, respectively. C_{aer} is called aerosol correction term and is a function of the altitude:

$$C_{\text{aer}} = R_{\text{aer}} q_A^2(\lambda, z) \tag{5}$$

Values of this nondimensional parameter range between 1.04 and 1.08 for typical aerosol and background conditions at the considered region, where $C_{\text{aer}} = 1{,}00$ represents the absence of aerosols. In equation (5) C_{aer} is used to calculate the absolute air density through the ratio between lidar signal measured with the aerosol backscattering ratio and aerosol transmission (Chen et al., 2004). The 11-year period here considered includes the Calbuco eruption during April 2015. After the eruption, an aerosol layer of high values of scattering ratio between 18 and 21 km spreading the Southern Hemisphere was observed by The Cloud-Aerosol Lidar with Orthogonal Polarization on board the Cloud-Aerosol Lidar and Infrared Pathfinder Satellite Observation (Bègue et al., 2017). However, 4 months after the eruption the scattering ratio values above 25 km remain similar to that before the eruption. An analysis was performed through the complete lidar data set to compare T profiles with and without aerosol contribution. The estimated aerosol load corresponded to background conditions under a bias lower than 4%. The algorithm provided T profiles with and without aerosol corrections, yielding a bias between both profiles on average lower than 4%. Finally, the lidar signal corrected is dominated fundamentally by Rayleigh scattering and a new temperature retrieval is performed following equations (1) and (4).

The temporal resolution of the photon counting system is 1 min, but an integration of at least 20 min is needed to improve the SNR. For the present data, two different approaches were used to integrate photon counting: (1) by integrating during the complete measuring interval and (2) by considering only a 20-min integration interval. The first approach provides a unique profile $T(z)$ and the best SNR, where the averaged value of GW activity can be extracted. The second approach provides $T\,(z, t)$, thus allowing to investigate GW periods and the vertical propagation direction.

Table 2
Some Characteristics of the Instruments Used

	Río Gallegos lidar	GPS RO	SABER
Vertical resolution	0.15 km	0.1–1.4 km	0.5–2 km
Horizontal resolution	--	150 km	300 km
Temporal resolution	20 min	--	--
Vertical range	20–50 km	0–40 km	20–120 km

Note. SABER = Sounding of the Atmosphere using Broadband Emission Radiometry; GPS = Global Positioning System; RO = radio occultation.

3. Satellite Data

Two satellite-based T data sets were used to compare the calculated GW activity with the one resulting from the lidar measurements: (1) the GPS RO limb sounding technique and (2) the Sounding of the Atmosphere using Broadband Emission Radiometry (SABER) on board Thermosphere Ionosphere Mesosphere Energetics Dynamics (TIMED) satellite. Table 2 presents a brief summary of the instruments used.

3.1. GPS RO

During a RO event, the GPS signal traverses the atmospheric limb up to a low Earth orbit satellite rising or setting behind the Earth. The GPS RO technique provides vertical profiles of atmospheric properties such as refractivity, from which ρ, p, and T are derived in the altitude range 0–40 km (see, e.g., Kursinski et al., 1997). The vertical resolution of RO profiles ranges from 0.1 km in the lower troposphere to 1.4 km in the stratosphere. Nevertheless, postprocessed profiles are available from near the surface up to 40 km, interpolated every 0.1 km. The horizontal resolution is about 150 km along the line of sight (LOS) defined between the GPS and low Earth orbit satellites. The GPS RO technique has global coverage, all-weather and all-time capability, sub-Kelvin T accuracy, high vertical resolution~~s~~, and long-term stability. The present work considers data from the COSMIC, from April 2006 to May 2014 (Anthes et al., 2008), CHAMP, between August 2005 and October 2008 (Schmidt et al., 2004), and the Global Navigation Satellite System Receiver for Atmospheric Sounding instrument on board the European Organization for the Exploitation of Meteorological Satellites satellite MetOp-A, between October 2007 and December 2011 (Luntama et al., 2008). In this work we used reprocessed products COSMIC2013, CHAMP-2016, and Metopa-2016. The sensitivity of the GPS RO technique to a certain portion of the full spectrum of GW horizontal wavelength (λ_H) and vertical λ_Z depends on the relative orientation of the LOS and the wave vector to be detected (P. Alexander et al., 2008). GPS RO data have been previously used for a vast range of GW-related studies (de la Torre & Alexander, 2005). In the present work, GPS RO postprocessed data (product version 2010.2640) available at COSMIC Data Analysis and Archive Center are used.

3.2. TIMED/SABER

This satellite uses a 10-channel broadband limb-scanning infrared radiometer to provide vertical profiles of T, p, geopotential height, and volume mixing ratios for trace species, for example, O_3. SABER provides approximately 2,200 profiles per day, with a vertical resolution of approximately 2 km between 10- and 120-km height and a precision between 1 and 3 K (Remsberg et al., 2008). Due to the TIMED spacecraft's yaw cycle, the spatial coverage changes every 60 days to cover the poles alternately with coverage extending to 51°S and to 87°S during the north and south yaw, respectively. Several authors used SABER data for GW-related studies, including Ern et al. (2008) and John and Kumar (2013).

4. Data Processing

4.1. Lidar

Between August 2005 and December 2015, the lidar recorded 1,018 hr of high-resolution data during a total of 302 nights of observations. The mean measuring time (MT) is 3 hr 22 min. The reason for this relatively short MT is that the original purpose of the lidar station was the observation of the stratospheric ozone depletion and T vertical distribution during the evolution of the polar vortex, rather than GWs parameters. In addition, the great variability of cloud cover during nighttime prevents frequent extended measurements in the region. This mean MT of the lidar measurements is relatively short to record typical GW periods between 2 and 10 hr. Only 20 observations were recorded with a MT longer than 6 hr. As explained above, although the maximum resolution of the photon counting system is 1 min, an integration of at least 20 min is needed to improve the SNR. A smaller integration time introduces high amplitude noise above 50 km, which may be easily misinterpreted as belonging to the temperature variability, leading to an overestimation of the GW activity. The noise begins at the top of the profile, and, as the integration time is reduced, it propagates downward reducing the height interval where GW can be reasonably detected. A 20-min integration time is recommended to study GW temporal variability as well as their periods and propagation

Table 3
Number of Lidar Measurements/Geometric Mean Lidar Specific Potential Energy (PE) [J/kg] (See Below), as a Function of Season and Relative Position to the Polar Vortex Edge

	DJF	MAM	JJA	SON	Total
Total	27/4.32	46/4.87	70/5.99	159/6.34	302/5.84
Inside	0/ --	0/ --	10/6.92	35/8.10	45/7.82
Border	0/ --	0/ --	10 5.82	33/6.84	43/6.60
Outside	7/2.19	18/6.82	50/5.84	91/5.70	166/5.62
No vortex	20/5.48	28/3.86	0/ --	0/ --	48/4.49

Note. JJA = June-July-August; MAM = March-April-May; SON = September-October-November; DJF = December-January-February

directions. In the present work, these data are used for the first time to analyze GW activity and parameters. The lidar T data may be expressed as a function of altitude and time. The vertical resolution of the lidar acquisition system is 0.15 km, and T fluctuations are interpreted as GWs when their associated vertical wavelengths (λ_z) are equal to or greater than 0.9 km. For lower λ_z values, the fluctuations may be related to noise.

Every lidar measurement is classified according to its relative position to the polar vortex. The same methodology followed by Wolfram et al. (2012), who studied the unusual persistence of an ozone hole during 2009 in southern Argentina, is applied. The equivalent latitude (*EL*) represents the latitude that an air mass would have if the polar vortex would be centered at the South Pole. The *EL* allows a better characterization of an air mass in terms of its location relative to the polar vortex, rather than in terms of the geographical latitude. The potential vorticity (*PV*) is calculated from the MIMOSA (Modélisation Isentrope du transport Méso-échelle de l'Ozone Stratosphérique par Advection) high-resolution advection model (Hauchecorne et al., 2002). High values of *PV* horizontal gradient at the vortex edge indicate a partial mix of air masses belonging, respectively, to the inside and the outside of the vortex. In contrast, a low *PV* gradient inside or outside the vortex indicates that these are quite homogeneous regions (Lee et al., 2001). The *EL* values corresponding to the internal and external boundaries that limit the polar vortex edge can be calculated from *PV*. The vortex edge limit corresponds to the *EL* value with the largest *PV* gradient weighted by the wind module (Nash et al., 1996). Accordingly, the local extreme of its second derivative corresponds to the inner and outer boundaries of the vortex. Three different conditions may characterize each measurement, depending on its relative position inside, outside, or at the vortex edge. A fourth condition may be further proposed, corresponding to a more distended condition after the vortex collapse (which will be called No Vortex). This situation usually takes place during summer and early autumn. The *PV* at the 475 K isentropic level is used to calculate *EL* at the polar vortex boundaries and classify each measurement according to these four conditions. A similar classification was made by Duck et al. (2001) at Eureka station (80°N, 86°W), using National Centers for Environmental Prediction analyses. Table 3 shows the number of nights of observation as a function of season and the relative position to the polar vortex.

4.2. Satellite

Coincident lidar measurements and CHAMP, COSMIC, MetOp-A, and SABER events were used for comparison. The coincident criterion is all observations with midpoints located in the region 49.6°S–53.6°S, 66.8°W–71.8°W. A total of 2763 GPS RO (101 CHAMP, 356 MetOp-A, and 2306 COSMIC) and 3,646 SABER profiles were found. Restricting this selection to ±6 hr with respect to the midtime of each lidar measurement, the number of collocated profiles is reduced to 173 GPS RO (13 CHAMP, 24 MetOp-A, and 136 COSMIC) and 637 SABER.

5. Methodology for GW Analysis

As usual in any GW analysis, it is considered that

$$T(z,t) = T'(z,t) + T_B(z,t) \tag{6}$$

where T' and T_B are the fluctuation and background components of T, respectively. Any GW analysis is based on a proper extraction of vertical T' profiles. Incorrect filtering leads to an underestimation/overestimation of wave activity. The background determination sets the range of detectable λ_Z. Recently, Ehard et al. (2015) evaluated the most common filtering methods used for the extraction of $T'(z,t)$ from lidar measurements using synthetic data.

The presence of intermittent large amplitude MWs has been reported in the region considered (e.g., Plougonven et al., 2013). For this reason, it is not convenient to derive T_B from a nightly mean, as a stationary wave pattern relative to the ground may be expected to be dominant. A nightly mean would remove any

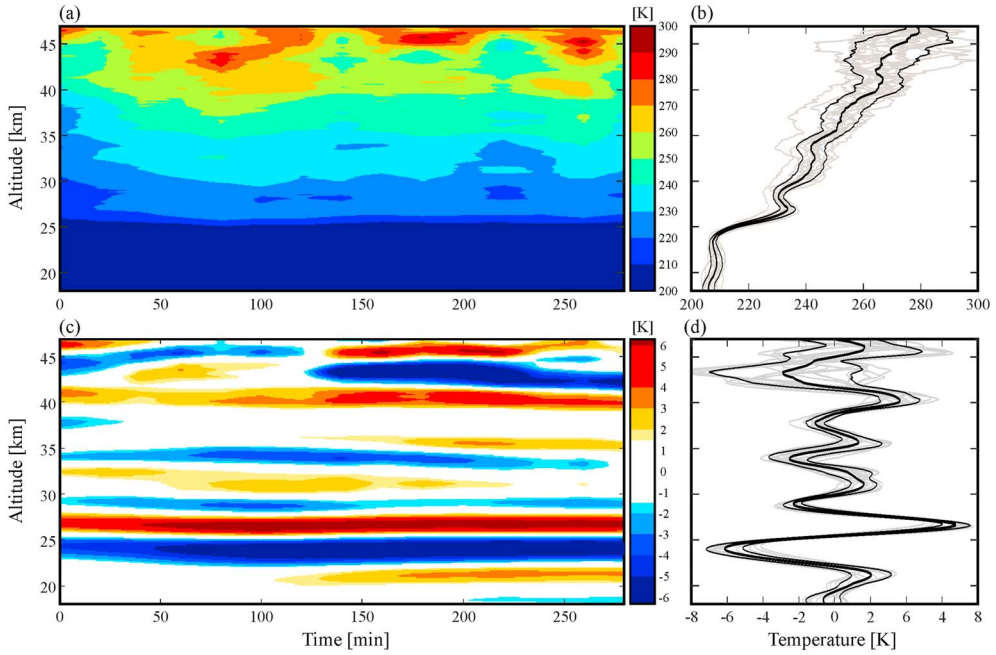

Figure 2. A lidar (a) T and (c) T' measurement as a function of altitude and time, respectively (18 November 2011). (b) T and (d) T' profiles as a function of altitude, every 20 min. The bold and light lines represent the mean and ±1 standard deviation.

stationary wave from the perturbation pattern, underestimating the GW activity. As an example, Figure 2 shows T and T' as a function of altitude and time. T' shows a typical stationary pattern with respect to the ground during the time span, with λ_z approximately equal to 5 km. This represents an example of how the removal of a nightly mean background to retrieve T' may lead to an important underestimation of GW activity. It is important to note that a ground-based lidar may observe GW at certain altitudes and not at others because the waves propagate out of the observational volume due to horizontal wind shear (Ehard et al., 2017).

The filtering procedure is as follows. First, the planetary wave contribution is removed, as proposed by Schmidt et al. (2016). In doing so, from each measured T profile we subtract interpolated ERA-Interim T data from the ECMWF. Planetary waves with zonal wave numbers 0–6 are removed. ERA Interim reanalysis data (Dee et al., 2011) are available with 0.7° × 0.7° × 6 hr longitude/latitude/time and 60 vertical levels from the surface up to 0.1 hPa. Then, a vertical detrending is applied to each profile and $T'(z,t_i)$ is obtained, following the method described by P. Alexander et al. (2011). A bandpass nonrecursive filter with lower and upper cut-offs, respectively, equal to 0.9 and 12 km, is applied. In profiles with multiple stratopauses, special care must be taken (see below section 6.2).

The mean PE is a magnitude broadly applied to the characterization of GW activity (e.g., de la Torre & Alexander, 2005). It is defined, between vertical levels, z_1 and z_2, as

$$PE = \frac{1}{2(z_2 - z_1)} \int_{z_1}^{z_2} \left(\frac{g}{N_2}\right)^2 \left(\frac{T'}{T}\right)^2 dz \tag{7}$$

N_z^2 is the Brunt Väisälä frequency:

$$N_z^2 = \frac{g}{T_B}\left(\frac{\delta T_B}{\delta z} + \frac{g}{c_p}\right) \tag{8}$$

where g is the gravitational acceleration and c_p is the isobaric specific heat capacity. The same filtering procedure was used for satellite data.

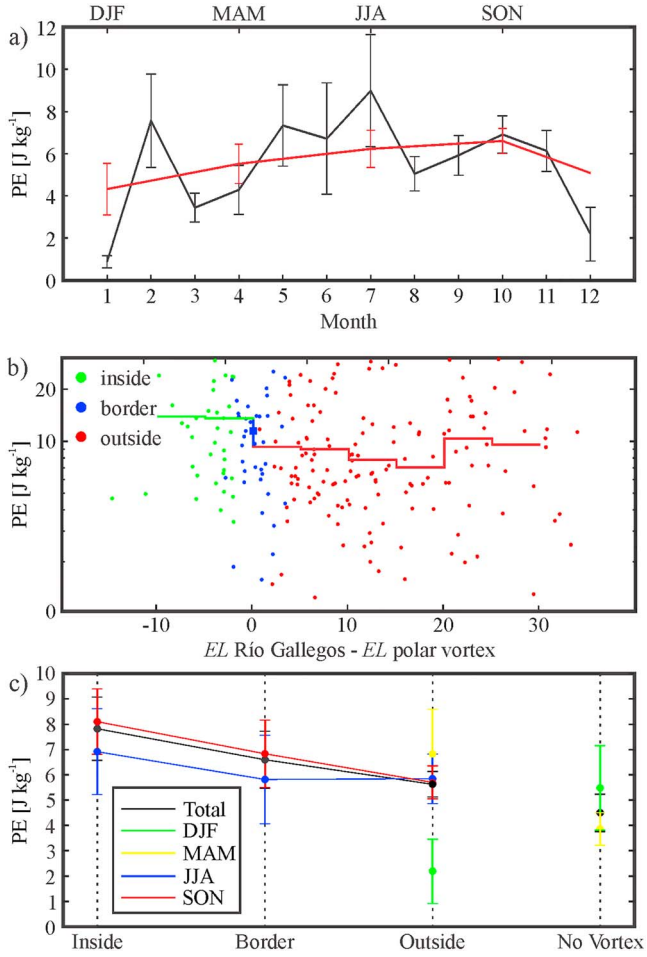

Figure 3. (a) GW monthly (black) and seasonal (red) geometric mean specific potential energy (*PE*) from lidar data, between 25 and 45 km. (b) *PE* from lidar data as a function of its position relative to the polar vortex boundary. The bold line represents the geometric mean of *PE*, for every 5° equivalent latitude (*EL*). The blue square denotes the geometric mean for the observations in the vortex edge. (c) Geometric mean of lidar *PE* measurements, classified by their relative position to the polar vortex and by season. JJA = June-July-August; MAM = March-April-May; SON = September-October-November; DJF = December-January-February.

6. Results of Analysis of GW

6.1. Lidar Data Analysis

Table 3 also summarizes the geometric mean of GW potential energy (*PE*) from the lidar measurements, classified by season and by the position relative to the polar vortex boundary (see below). As described by Baumgaertner and McDonald (2007), the geometric mean is a more convenient measure of *PE* variability than the arithmetic mean and will be applied here. The geometric mean of *PE* considering the four regions (inside, at the edge of the vortex, outside it, and without vortex) is larger during winter (June-July-August (JJA)) and spring (September-October-November, SON) than during summer (December-January-February, DJF) and autumn (March-April-May, MAM). The largest geometric mean of *PE* considering the complete time span is found inside the vortex and decreases monotonically at its edge, outside it, and when there is no vortex (only during DJF and MAM). During SON, the polar vortex weakens and advances northward, sometimes beyond Río Gallegos, during rapidly changing weather conditions. The polar vortex always crosses Río Gallegos from west to east. This situation usually lasts for 1 or 2 days and is followed by an increase in wind speed. During SON, the Río Gallegos station is more likely to lie inside the polar vortex (35 cases detected). During DJF and MAM, no measurements inside or at the polar vortex boundary were found. Outside the vortex, the lowest *PE* is found during DJF and the largest during MAM. This comparison at the vortex edge is hard to accomplish with limb satellite data, because each measurement is averaged out along hundreds of kilometers along the LOS and the localization of the vortex edge boundaries is unclear. This situation is critical for GPS RO profiles, where about 40% of the soundings have a LOS lying within 30° from the north-south axis. Figure 3a shows the monthly (black) and seasonal (red) geometric mean of lidar *PE*, integrated between 25 and 45 km, for the observation period considered. Although the maximum monthly geometric mean *PE* is found during July, the maximum seasonal geometric mean *PE* is found during SON. The minimum *PE* is found during DJF.

Figure 3b shows the nightly mean lidar *PE*, as a function of the position relative to the polar vortex boundary. The bold line represents the geometric mean of the lidar measurements for every 5° of *EL*. The blue square represents the geometric mean of the measurements corresponding to the edge region of the polar vortex. As stated before, the larger *PE* values are found when the lidar station lies inside the polar vortex and a secondary maximum is observed for $EL > 20°$. Nevertheless, no seasonal dependence is observed at the edge. Figure 3c shows the distribution of the geometric mean of nightly mean lidar *EP* as a function of season and position relative to the edge. The geometric mean for the complete measurement set (black line) is also shown.

6.2. Two Profiles Deserving Different Treatment: Multiple Stratopauses

Exceptionally, 2 from the 302 cases were obtained in the vicinity of the vortex edge. For these cases, air masses are partially mixed and the presence of apparent multiple stratopauses is seen. This makes it difficult to retrieve T_B. An example of multiple stratopauses is shown in Figure 4.

In this figure, *T* and *T'* are shown. As it can be seen, if the distance between both stratopauses is shorter than the upper filtering cutoff, the double stratopause turns out to be a part of the perturbation, instead of the background. This leads to an overestimation of *PE*. These cases require a different approach. It is not easy to discriminate a double stratopause from a high amplitude GW. In Figure 4c, the potential vorticity map at 475 K from MIMOSA indicates the position of the vortex edge situated above Río Gallegos. Along this lidar

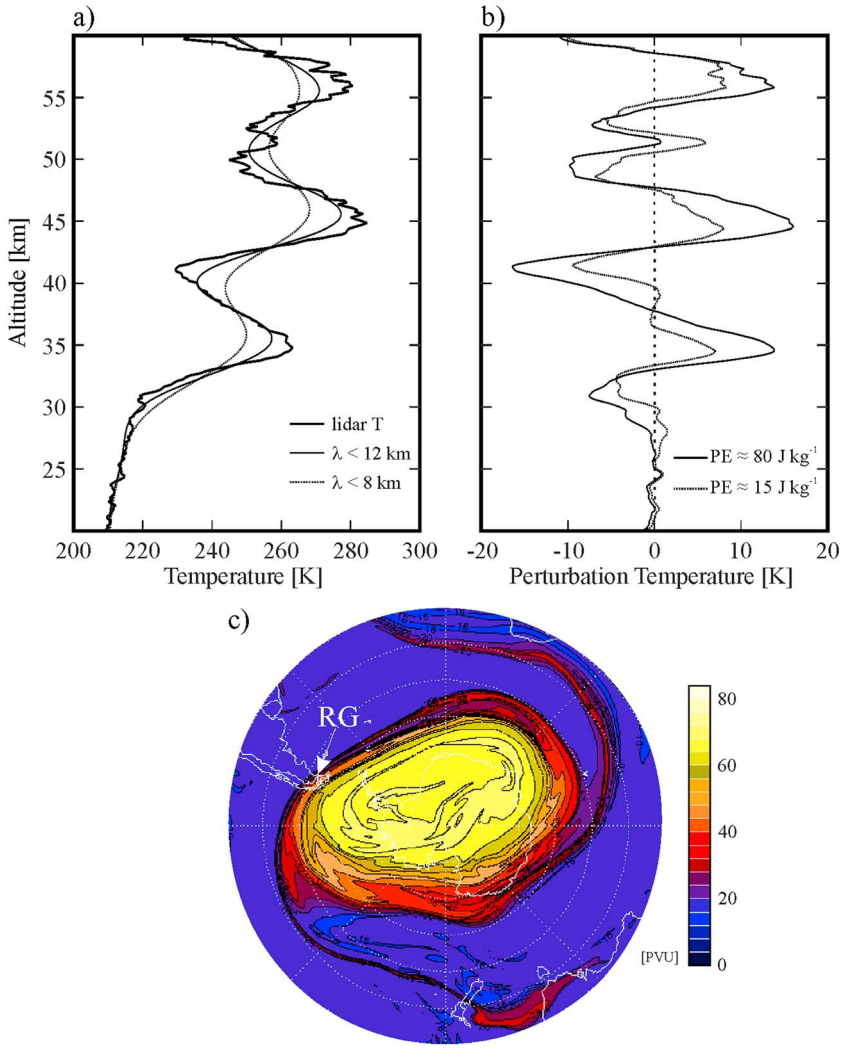

Figure 4. (a) *T* lidar profile and T_B, (b) *T'* corresponding to the use of two different filtering upper cutoffs (8 and 12 km) in order to isolate GW. If the distance between both stratopauses is shorter than the used cutoff, the *PE* is clearly overestimated. (c) Potential vorticity (pvu) at 475 K (from MIMOSA). GW = gravity wave; MIMOSA = Modélisation Isentrope du transport Méso-échelle de l'Ozone Stratosphérique par Advection; JJA = June-July-August; MAM = March-April-May; SON = September-October-November; DJF = December-January-February.

measurement, the structure of the vortex, as it usually happens, slightly changes at different altitudes (not shown), then the lidar sounding path lies at different positions relative to the edge of the vortex. This explains the abrupt changes along this singular *T* profile.

6.3. Spectral Distribution of GW Activity From the Lidar Observations

The λ_z distribution derived from the lidar measurements is observed from a fast Fourier transform applied to each *T'* profile, between 25- and 45-km height. Figure 5a shows the power spectral density (PSD) of *T'* as a function of the vertical wave number. This magnitude has been largely observed in the literature as a measure of wave energy distribution from a given GW ensemble (e.g., de la Torre et al., 1994).

The mean *T'* PSD follows the expected −3 slope for saturated spectra in the λ_z range [1–8] km. The histogram in Figure 5b shows prevailing λ_z modes from the set of measurements. Main modes with λ_z between 4.5 and 7 km are observed. It must be remarked that λ_z values obtained from lidar measurements do not undergo the systematic and sometimes very considerable distortions derived from slanted and/or not instantaneous measurements. These deviations characterize other experimental platforms, as limb sounding data or radio

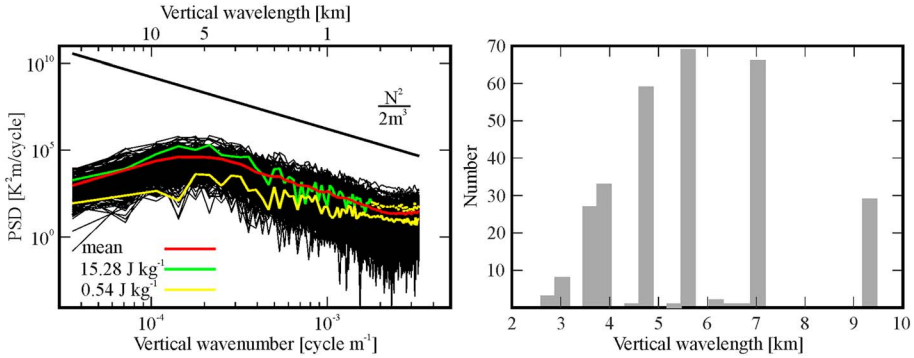

Figure 5. (a) Power spectral density as a function of the vertical wave number m for the 302 lidar T' measurements. The red line represents the mean, whereas the green and yellow lines, respectively, represent arbitrary selected high and low GW activity measurements. The universal saturation line $N^2/2m$ is included for reference. (b) Histogram of the main prevailing λ_z modes. GW = gravity wave; PSD = power spectral density.

soundings. Accordingly, the results shown in Figure 5 involve the *real* rather than *apparent* λ_z values (de la Torre et al., 2018).

6.4. Satellite Data Analysis

The lidar measurements are compared with collocated SABER and GPS RO data within the selected region (49.6°S–53.6°S, 66.8°W–71.8°W; Figures 6 and 7, respectively). For lidar and SABER data, *PE* is integrated between 25 and 45 km. For GPS RO, a different integration altitude between 20 and 30 km is considered. As Luna et al. (2013) pointed out, GWs from RO data are not wrong but are less reliable above 30-km height than below this altitude. Up to 30 km, the results will probably remain solid. The more our results depart upward from 30 km, the more cautious we should be about being conclusive. These authors obtained this conclusion after considering different integration altitude intervals including T measurements above 30 km. They attributed the resulting *PE* uncertainty to spurious oscillations introduced by the initialization procedure of GPS RO profiles, which injects artificial additional energy to the profiles above 30 km (Luna et al., 2013; Figure 4). At this point, it is important to remember that different instruments show different spectral windows of the GW spectrum, yielding complementary observations. In particular, limb observations are strongly dependent on the relative orientation between the LOS and the wavefronts to be detected. In addition to the attenuation in the measured amplitudes (P. Alexander et al., 2008), a significant distortion in the measured wavelengths is also expected. This is the case for soundings other than in vertical and horizontal directions (de la Torre et al., 2018). Therefore, these λ_Z distortions are not expected from lidar measurements.

On average, it may be seen (Figure 3a) that lidar observations provide larger *PE* values than limb sounding measurements (Figures 6a and 7a). Lidar *PE* is approximately 4 times larger. In Figures 6a and 7a, a 30-day running mean is applied to daily averaged *PE* values. This procedure is not possible in Figure 3a, due to the considerably nonhomogeneous time series and frequent windows with missing consecutive daily data.

Figures 6b and 7b show the Morlet continuous wavelet transform (CWT) from the interpolated SABER and GPS RO *PE* time series, respectively. As mentioned above, before applying the CWT, all SABER and GPS RO data were interpolated on a daily basis and a 30 day moving average was applied. From SABER data (Figure 6b), a clear annual cycle of *PE* is observed, with a maximum during late winter and early spring along the time span. A less intense semiannual cycle is also observed during the first half of the time span. A second intense signal is perceived at a period slightly longer than 4 years. A Morlet CWT from GPS RO data (Figure 7b) shows an intense semiannual cycle and a weaker mode around 1.5 years. A second intense signal is observed within a period slightly shorter than 4 years. It could be concluded that three main modes are captured from SABER and in GPS RO data, in the upper and lower stratosphere, respectively. Two interesting features should be remarked in *PE* from these collocated satellite observations: the systematic 3- to 4-year oscillation and the minimum/maximum observed every year in September from GPS RO/SABER.

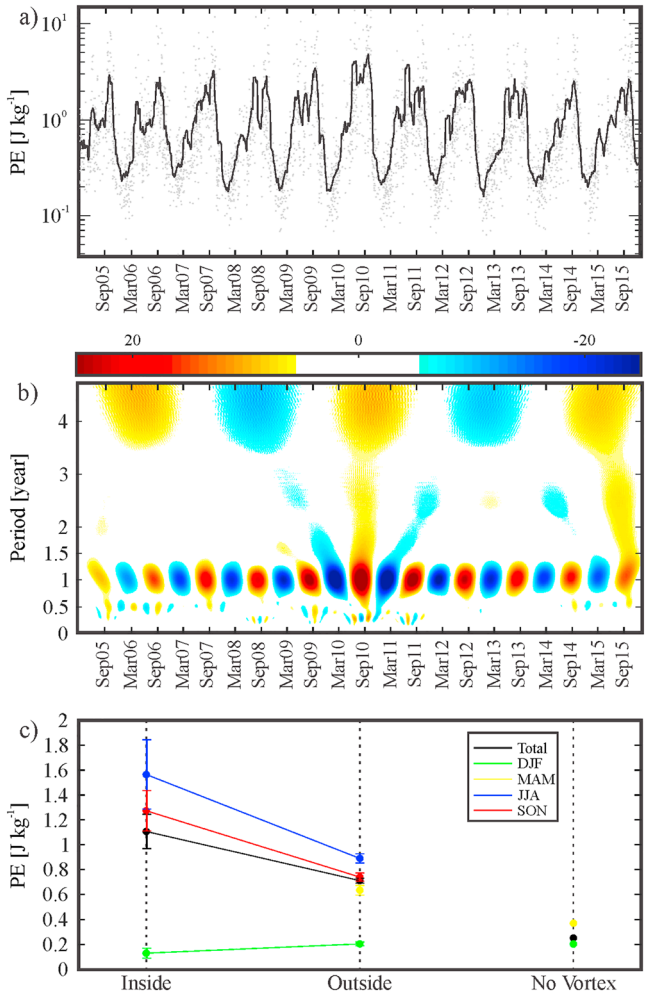

Figure 6. (a) GW specific potential energy (*PE*) from SABER data (dots), between 25 and 45 km. The black line is a 30-day moving average. (b) Morlet continuous wavelet transform from the interpolated SABER *PE* time series. (c) Geometric mean of SABER *PE* measurements, classified by their relative position to the polar vortex and by season. GW = gravity wave; SABER = Sounding of the Atmosphere using Broadband Emission Radiometry; JJA = June-July-August; MAM = March-April-May; SON = September-October-November; DJF = December-January-February.

7. Discussion and Observed Variability of GW Activity

The GW activity results presented in section 5 exhibit diverse and not necessarily coincident features, which depend mainly on the experimental platform here presented. Our lidar data gaps prevent the continuous observation of time variability along the 11 years considered, but the period covered by this instrument is not usually found in the literature. An analysis similar to ours was performed at Eureka (80°N, 86°W) by Duck et al. (2001), who used National Centers for Environmental Prediction analyses to classify the measurements relative to the vortex. However, in the Arctic they found a larger *PE* at the polar vortex edge boundary during the Northern Hemisphere winter and lower *PE* values both inside and outside. Differences with respect to those of Duck et al. (2001) may in part be attributed to the presence of the Andes Mountains at the southern tip of the continent, surrounded by the oceanic mass. Other lidar studies, from measurements performed during considerably shorter time periods in high southern latitudes, may be mentioned. Kogure et al. (2017) calculated *EP* at altitudes of 15–70 km, from *T* profiles obtained by a Rayleigh/Raman lidar at Syowa Station (69°S, 40°E) from May 2011 to October 2013, with the exception of the summer months. According to their results, *EP* was larger in winter than in spring and fall and, in 2012, at altitudes below 30 km. The values of *EP* in October 2012 were smaller at 35–60 km and larger at 20–35 km than those in October 2011 and 2013. This difference in *EP* was most probably attributed to different seasonal variations of zonal winds. Wind filtering of GW with small phase speeds could be significant in early spring. Kaifler, Lübken, et al. (2015), from 2,310 hr of measurements during 2011 and 2012, investigated the seasonal variations in GW activity. In comparison to our satellite results, in the stratosphere they found GW activity with large seasonal variations and additional periods accounting for this variability: a double peak in winter and a minimum in summer. In these last two studies, no interannual variability was reported due to the short period considered. S. P. Alexander et al. (2011), from data retrieved from a Rayleigh lidar at Davis, Antarctica (69°S, 78°E) during the 2007 and 2008 winters, found stratospheric *PE* with a weaker correlation with stratospheric winds at Davis than that reported in the Arctic. The seasonal cycle of GW activity was evident throughout the upper stratosphere/lower mesosphere, with a peak activity observed during winter. The *PE* and vertical wave number PSD at Davis were similar to those recorded at other high-latitude sites.

From GPS RO data, S. P. Alexander et al. (2009) found a result similar to that of this study during the 2007 austral spring. They found that *T* variance values within the vortex boundary region between the 400 and 600 K isentropes are twice as large as those found outside the vortex. Wright et al. (2016) performed an intercomparison among several nadir and limb sounding instruments and radio soundings in the southern tip of South America. In particular, they obtained a very good match between GW activity obtained from both limb soundings, with *PE* exhibiting a clear annual variability with maxima during spring and winter.

From the different main sources of GW, the clear-sky conditions imposed to the lidar measurements presented in this study exclude the consideration of a relatively significant generation of convective waves. As stated before, perhaps the strongest candidate among the remaining possible sources consists in mountain forcing. We must expect possible sporadic (or systematic) imbalances in the flow between mass and momentum, capable of generating inertia-GWs through geostrophic adjustment, as the atmosphere tries to restore equilibrium (see, e.g., Plougonven & Zhang, 2014; Zhang, 2004; Zhang et al., 2000). In doing so, we may consider different available methods. Each of them involves the calculation of a specific parameter, with its advantages and disadvantages (cross-stream component of the Lagrangian Rossby number ($Ro_{\perp}$), Psi

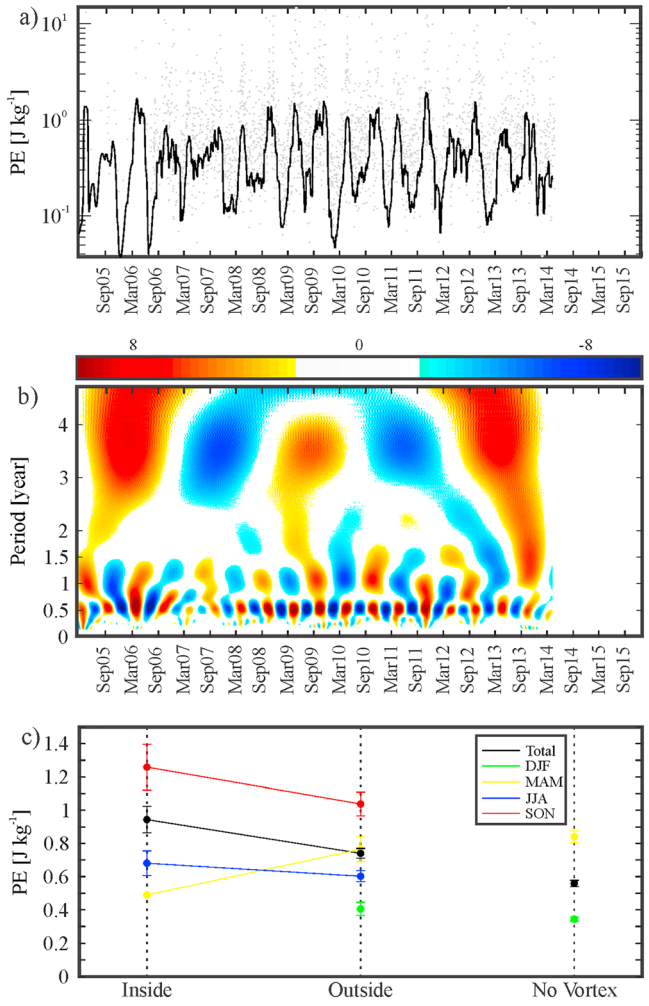

Figure 7. (a) GW-specific potential energy (*PE*) from GPS RO data, between 20 and 30 km (dots). The black line is a 30-day moving average. (b) Morlet continuous wavelet transform from the interpolated GPS RO *PE* time series. (c) Geometric mean of GPS RO *PE* measurements, classified by their relative position to the polar vortex and by season. GW = gravity wave; JJA = June-July-August; MAM = March-April-May; SON = September-October-November; DJF = December-January-February; GPS = Global Positioning System; RO = radio occultation.

vector, generalized omega equation, or nonlinear balance equation). Following de la Torre et al. (2006), we analyzed the $Ro_{\perp}$ distribution from reanalysis and from the simulated geopotential and velocity data. When a geostrophic imbalance (e.g., Fritts & Alexander, 2003) coexists with other sources, $Ro_{\perp}$, defined by the ratio of the component of the ageostrophic wind normal to the flow to the observed wind speed, is expected to be greater than 0.5, and a further analysis should probably be more intricate. In the present study, in Figure 8 we compare two representative lidar profiles as a function of time, corresponding to dates 16 September 2011 and 18 November 2011 (already shown in Figure 2). At lower levels, the second profile suggests a more prevailing MW structure than the first one (Figures 8a and 8c). For both cases, $Ro_{\perp}$ calculated at 250 hPa (Figures 8b and 8d) is clearly <0.5 at jet pressure levels. According to these two examples, inertia-GWs originated in possible flux unbalance and departure from geostrophic equilibrium could be discarded. The observed GW structures should be conceivably limited to stationary waves and/or to possible contributions from other sources, as fronts (Richter et al., 2010), convection (Choi & Chun, 2013), small islands (Hoffmann et al., 2013), and large eddy growth instabilities at 500 hPa in the storm tracks (Hendricks et al., 2014), and generated in partial reflection/nonlinear processes (Sato et al., 2012).

In addition to a discussion of the available sources, regarding GW propagation it must be kept in mind that in the region considered, upward and downward GWs are expected to be strongly deviated by vertical and horizontal (poleward) refraction in the presence of the jet (Jiang et al., 2013; Pulido et al., 2012).

A possible explanation regarding the 3- to 4-year period may be proposed as follows. Patterns of low-frequency variability in Southern Hemisphere circulation, mostly extratropical in origin, but which can interact with El Niño–Southern Oscillation (ENSO), are dominated by the zonally symmetric *high-latitude mode* or Antarctic Oscillation (Carleton, 2003). The Antarctic Oscillation involves an alternation of atmospheric mass between middle and high southern latitudes. A zonally asymmetric mode of wave number 1 is represented by an oscillation in pressure/height between Australian and South American sectors. A significant wave number 2 oscillation in the coupled atmosphere-ocean-ice system or Antarctic circumpolar wave has a similar periodicity to ENSO (e.g., Llamedo et al., 2016) and is strongest in the Pacific-SW Atlantic sectors. The similar periodicity between the ENSO and the *PE* variability deserves further investigation to inspect a possible relationship between these observed features. The enhanced wave activity inside the polar vortex as compared to the one observed outside it (already noted from lidar data in Figure 3) is captured again from both satellite data. As mentioned before, in Figures 6c and 7c the vortex edge was not considered, due to the difficulty to identify satellite events strictly at this narrow location.

8. Summary

The 302 nights of Rayleigh lidar observations were used to monitor the GW activity in terms of its specific potential energy, above Río Gallegos, between 2005 and 2015. The lidar measurements were complemented with limb satellite-based GPS RO and SABER data collocated within the surrounding region 49°S–53°S, 67°W–72°W. These observations, originally performed to study the stratospheric ozone depletion and *T* vertical distribution during the evolution of the polar vortex, are used for the first time in a GW analysis. The great variability of cloud cover during nighttime prevents frequent extended measurements in the region. Three different conditions may characterize each measurement, depending on its relative position: inside,

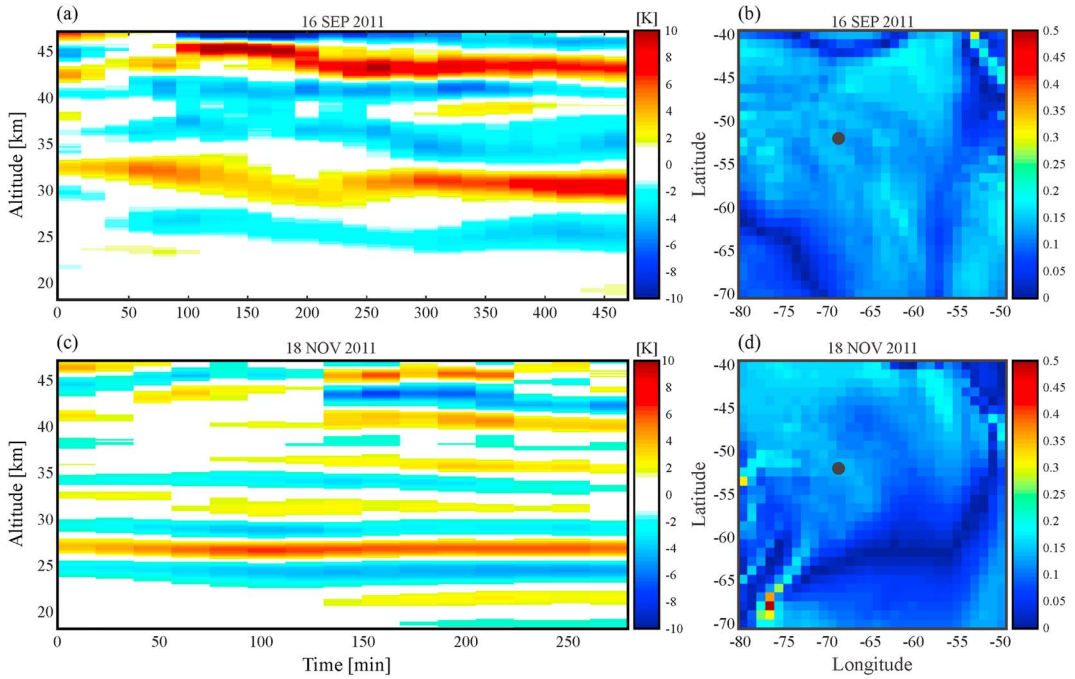

Figure 8. Two representative lidar profiles as a function of time, corresponding to dates (a) 16 September 2011 and (c) 18 November 2011 (already shown in Figure 2). $Ro_{\perp}$ calculated for both cases at 250 hPa (b and d, respectively, see text), indicating the general low imbalance of the flux. The black circle indicates the lidar location.

outside, or at the vortex edge. A fourth possibility corresponds to the more distended condition arising after vortex collapse. This situation usually occurs during summer and early autumn. In general, the geometric mean of *PE* is larger during winter (June-July-August JJA) and spring (SON) than during summer (DJF) and autumn (MAM). The largest geometric mean of *PE* considering the complete time span is found inside the vortex and decreases monotonically at the edge of it, outside it, and when there is no vortex (only during DJF and MAM). During DJF and MAM, no measurements inside or at the polar vortex boundary were found. Outside the vortex, the lowest *PE* is found during DJF and the largest during MAM. The lidar measurements are compared with collocated SABER and GPS RO data within the selected region. The different instruments show different spectral windows of the GW spectrum, yielding complementary observations. In particular, limb observations are strongly dependent on the relative orientation between the LOS and the wavefronts to be detected. In addition to the attenuation in the measured amplitudes, a significant distortion in the measured wavelengths is also expected. This is the case for soundings other than in vertical and horizontal directions. These λ_Z distortions are not expected from lidar measurements. On average, it can be seen that lidar observations provide larger *PE* values than limb sounding measurements, as expected. Although the lidar data gaps prevent a continuous observation of the time variability of *PE*, the 11 years considered represent an improvement with respect to previous lidar studies in the region considered.

From SABER data, a clear annual cycle of *PE* is observed, with a maximum during late winter and early spring along the time span. A less intense semiannual cycle is also observed during the first half of the time span. A second intense signal is appreciated at a period slightly longer than 4 years. GPS RO data show an intense semiannual cycle, a weaker mode around 1.5 years and a second intense signal in a period slightly shorter than 4 years. The three distinct modes are captured from SABER and in GPS RO data, at the upper and lower stratosphere, respectively. A possible relation of the 3- to 4-year oscillation with the ENSO variability is suggested, as patterns of low-frequency variability in Southern Hemisphere circulation, mostly extratropical in origin, can interact with it. A systematic minimum/maximum in September from GPS RO/SABER is observed. The enhanced wave activity inside the polar vortex, as compared to the one observed outside it, is captured from both lidar and satellite data. In addition to the expected generation of GW activity

by the orographic forcing mechanism, the analysis of two arbitrary cases yielded no indications of flux imbalance and nonstationary GW. Obviously, a detailed climatology considering every measured profile would be needed to provide conclusions regarding the relative importance of this and/or other proposed GW sources.

The PSD of T', as a function of λ_z, follows the expected -3 slope for saturated spectra in the λ_z range [1–8] km, with prevailing λ_z modes between 4.5 and 7 km. λ_z, as obtained from lidar measurements, does not suffer from the systematic and considerable distortions expected in other experimental setups due to slanted measurements.

Since December 2017, a second lidar station is operating at the Argentinean city of Río Grande (53.5 S, 67.4 W), located at 250 km to the south of Río Gallegos. This new Rayleigh lidar, belonging to the Institute of Atmospheric Physics of the German Aerospace Center, allows to retrieve middle atmospheric profiles during operational periods identical to those at Río Gallegos, as well as the analysis of GW sources and propagation simultaneously inside and/or outside the polar vortex.

Acknowledgments
Manuscript prepared under grants CONICET PIP11220120100034 and ANPCYT PICT2013-1097. P. Llamedo, J. Salvador, A. de la Torre, J. Quiroga, P. Alexander, and R. Hierro are members of CONICET. This research was supported by the Science and Technology Research Partnership for Sustainable Development (SATREPS), Japan Science and Technology Agency (JST), and Japan International Cooperation Agency (JICA). The DIAL construction and maintenance since 2005 were supported by projects from ANPCYT, CONICET, and CNRS. MIMOSA model data were downloaded from aeris-data.fr/mimosa. According to AGU data policy, an archive weblink to the lidar data may found at https://figshare.com/s/ca19a838a78ca5afe1d4. GPS RO and TIMED/SABER data were downloaded, respectively, from http://cdaac-www.cosmic.ucar.edu/cdaac-products.html and http://saber.gats-inc.com/browse_data.php.

References

Alexander, P., de la Torre, A., & Llamedo, P. (2008). Interpretation of gravity wave signatures in GPS radio occultations. *Journal of Geophysical Research*, *113*, D16117. https://doi.org/10.1029/2007JD009390

Alexander, P., de la Torre, A., Llamedo, P., Hierro, R., Schmidt, T., Haser, A., & Wickert, J. (2011). A method to improve the determination of wave perturbations close to the tropopause by using a digital filter. *Atmospheric Measurement Techniques*, *4*(9), 1777–1784. https://doi.org/10.5194/amt-4-1777-2011

Alexander, P., Luna, D., Llamedo, P., & de la Torre, A. (2010). A gravity waves study close to the Andes mountains in Patagonia and Antarctica with GPS radio occultation observations. *Annales de Geophysique*, *28*(2), 587–595. https://doi.org/10.5194/angeo-28-587-2010

Alexander, S. P., Klekociuk, A. R., & Murphy, D. J. (2011). Rayleigh lidar observations of gravity wave activity in the winter upper stratosphere and lower mesosphere above Davis, Antarctica (69°S, 78°E). *Journal of Geophysical Research*, *116*, D13109. https://doi.org/10.1029/2010JD015164

Alexander, S. P., Klekociuk, A. R., & Tsuda, T. (2009). Gravity wave and orographic wave activity observed around the Antarctic and Arctic stratospheric vortices by the COSMIC GPS-RO satellite constellation. *Journal of Geophysical Research*, *114*, D17103. https://doi.org/10.1029/2009JD011851

Alexander, S. P., Sato, K., Watanabe, S., Kawatani, Y., & Murphy, D. J. (2016). Southern Hemisphere extratropical gravity wave sources and intermittency revealed by a middle-atmosphere general circulation model. *Journal of the Atmospheric Sciences*, *73*(3), 1335–1349, https://doi.org/10.1175/JAS-D-15-0149.1

Anthes, R. A., Bernhardt, P. A., Chen, Y., Cucurull, L., Dymond, K. F., Ector, D., et al. (2008). The COSMIC/FORMOSAT-3 MISSION early results. *American Meteorological Society*, *89*(3), 313–334. https://doi.org/10.1175/BAMS-89-3-313

Baumgaertner, A. J. G., & McDonald, A. J. (2007). A gravity wave climatology for Antarctica compiled from Challenging Minisatellite Payload/Global Positioning System (CHAMP/GPS) radio occultations. *Journal of Geophysical Research*, *112*, D05103. https://doi.org/10.1029/2006JD007504

Bègue, N., Vignelles, D., Berthet, G., Portafaix, T., Payen, G., Jégou, F., et al. (2017). Long-range transport of stratospheric aerosols in the Southern Hemisphere following the 2015 Calbuco eruption. *Atmospheric Chemistry and Physics*, *17*, 15,019–15,036, https://doi.org/10.5194/acp-17-15019-2017

Bencherif, H., Portafaix, T., Baray, J. L., Morel, B., Baldy, S., Leveau, J., & Diab, R. (2003). LIDAR observations of lower stratospheric aerosols over South Africa linked to large scale transport across the southern subtropical barrier. *Journal of Atmospheric and Solar - Terrestrial Physics*, *65*(6), 707–715. https://doi.org/10.1016/S1364-6826(03)00006-3

Cao, B., Heale, C. J., Guo, Y., Liu, A. Z., & Snively, J. B. (2016). Observation and modeling of gravity wave propagation through reflection and critical layers above Andes Lidar Observatory at Cerro Pachón, Chile. *Journal of Geophysical Research: Atmospheres*, *121*, 12,737–12,750. https://doi.org/10.1002/2016JD025173

Carleton, A. M. (2003). Atmospheric teleconnections involving the Southern Ocean. *Journal of Geophysical Research*, *108*(C4), 8080. https://doi.org/10.1029/2000JC000379

Chen, W. N., Tsao, C. C., & Nee, J. B. (2004). Rayleigh lidar temperature measurements in the upper troposphere and lower stratosphere. *Journal of Atmospheric and Solar - Terrestrial Physics*, *66*(1), 39–49. https://doi.org/10.1016/j.jastp.2003.09.014

Choi, H.-J., & Chun, H.-Y. (2013). Effects of convective gravity wave drag in the Southern Hemisphere winter stratosphere. *Journal of the Atmospheric Sciences*, *70*(7), 2120–2136. https://doi.org/10.1175/JAS-D-12-0238.1

de la Torre, A., & Alexander, P. (2005). Gravity waves above Andes detected from GPS radio occultation temperature profiles: Mountain forcing? *Geophysical Research Letters*, *32*, L17815. https://doi.org/10.1029/2005GL022959

de la Torre, A., Alexander, P., Hierro, R., Llamedo, P., Rolla, A., Schmidt, T., & Wickert, J. (2012). Large-amplitude gravity waves above the southern Andes, the Drake Passage and the Antarctic Peninsula. *Journal of Geophysical Research*, *117*, D02106. https://doi.org/10.1029/2011JD016377

de la Torre, A., Alexander, P., Llamedo, P., Menéndez, C., Schmidt, T., & Wickert, J. (2006). Gravity waves above the Andes detected from GPS radio occultation temperature profiles: Jet mechanism? *Geophysical Research Letters*, *33*, L24810. https://doi.org/10.1029/2006GL027343

de la Torre, A., Alexander, P., Schmidt, T., Llamedo, P., & Hierro, R. (2018). On the distortions in calculated GW parameters during slanted atmospheric soundings. *Atmospheric Measurement Techniques*, *11*(3), 1363–1375, https://doi.org/10.5194/amt-11-1363-2018

de la Torre, A., Giraldez, A., & Alexander, P. (1994). Saturated gravity wave spectra measured with balloons in Mendoza (Argentina). *Geophysical Research Letters*, *21*, 2039–2042. https://doi.org/10.1029/94GL01589

Dee, D. P., Uppala, S. M., Simmons, A. J., Berrisford, P., Poli, P., Kobayashi, S., et al. (2011). The ERA-Interim reanalysis: Configuration and performance of the data assimilation system. *Quarterly Journal of the Royal Meteorological Society*, *137*(656), 553–597. https://doi.org/10.1002/qj.828

Duck, T. J., Whiteway, J. A., & Carswell, A. I. (1998). Lidar observations of gravity wave activity and Arctic stratospheric vortex core warming. *Geophysical Research Letters*, *25*, 2813–2816. https://doi.org/10.1029/98GL02113

Duck, T. J., Whiteway, J. A., & Carswell, A. I. (2001). The gravity wave-Arctic stratospheric vortex interaction. *Journal of the Atmospheric Sciences*, *58*(23), 3581–3596. https://doi.org/10.1175/1520-0469(2001)058<3581:TGWASV>2.0.CO;2

Ehard, B., Kaifler, B., Dörnbrack, A., Preusse, P., Eckermann, S. D., Bramberger, M., et al. (2017). Horizontal propagation of large-amplitude mountain waves into the polar night jet. *Journal of Geophysical Research: Atmospheres*, *122*, 1423–1436. https://doi.org/10.1002/2016JD025621

Ehard, B., Kaifler, B., Kaifler, N., & Rapp, M. (2015). Evaluation of methods for gravity wave extraction from middle-atmospheric lidar temperature measurements. *Atmospheric Measurement Techniques*, *8*(11), 4645–4655. https://doi.org/10.5194/amt-8-4645-2015

Ern, M., Preusse, P., Krebsbach, M., Mlynczak, M. G., & Russell, J. M. III (2008). Equatorial wave analysis from SABER and ECMWF temperatures. *Atmospheric Chemistry and Physics*, *8*(4), 845–869. https://doi.org/10.5194/acp-8-845-2008

Fernald, F. G. (1984). Analysis of atmospheric lidar observations: Some comments. *Applied Optics*, *23*(5), 652. https://doi.org/10.1364/AO.23.000652

Fritts, D. C., & Alexander, M. J. (2003). Gravity wave dynamics and effects in the middle atmosphere. *Reviews of Geophysics*, *41*(1), 1003. https://doi.org/10.1029/2001RG000106

Fritts, D. C., Smith, R. B., Taylor, M. J., Doyle, J. D., Eckermann, S. D., Dörnbrack, A., et al. (2016). The Deep Propagating Gravity Wave Experiment (DEEPWAVE): An airborne and ground-based exploration of gravity wave propagation and effects from their sources throughout the lower and middle atmosphere. *Bulletin of the American Meteorological Society*, *97*(3), 425–453, https://doi.org/10.1175/BAMS-D-14-00269.1

Geller, M. A., Alexander, M. J., Love, P. T., Bacmeister, J., Ern, M., Hertzog, A., et al. (2013). A comparison between gravity wave momentum fluxes in observations and climate models. *Journal of Climate*, *26*(17), 6383–6405. https://doi.org/10.1175/JCLI-D-12-00545.1

Gross, M. R., McGee, T. J., Ferrare, R. A., Singh, U. N., & Kimvilakani, P. (1997). Temperature measurements made with a combined Rayleigh–Mie and Raman lidar. *Applied Optics*, *36*(24), 5987–5995. https://doi.org/10.1364/AO.36.005987

Hauchecorne, A., & Chanin, M. L. (1980). Density and temperature profiles obtained by lidar between 35 and 70 km. *Geophysical Research Letters*, *7*, 565–568. https://doi.org/10.1029/GL007i008p00565

Hauchecorne, A., Godin, S., Marchand, M., Hesse, B., & Souprayen, C. (2002). Quantification of the transport of chemical constituents from the polar vortex to midlatitudes in the lower stratosphere using the high-resolution advection model MIMOSA and effective diffusivity. *Journal of Geophysical Research*, *107*(D20), 8289. https://doi.org/10.1029/2001JD000491

Hendricks, E. A., Doyle, J. D., Eckermann, S. D., Jiang, Q., & Reinecke, P. A. (2014). What is the source of the stratospheric gravity wave belt in austral winter? *Journal of the Atmospheric Sciences*, *71*(5), 1583–1592. https://doi.org/10.1175/JAS-D-13-0332.1

Hindley, N. P., Wright, C. J., Smith, N. D., & Mitchell, N. J. (2015). The southern stratospheric gravity wave hot spot: Individual waves and their momentum fluxes measured by COSMIC GPS-RO. *Atmospheric Chemistry and Physics*, *15*(14), 7797–7818. https://doi.org/10.5194/acp-15-7797-2015

Hoffmann, L., Grimsdell, A. W., & Alexander, M. J. (2016). Stratospheric gravity waves at Southern Hemisphere orographic hotspots: 2003–2014 AIRS/Aqua observations. *Atmospheric Chemistry and Physics*, *16*(14), 9381–9397. https://doi.org/10.5194/acp-16-9381-2016

Hoffmann, L., Xue, X., & Alexander, M. J. (2013). A global view of stratospheric gravity wave hotspots located with Atmospheric Infrared Sounder observations. *Journal of Geophysical Research: Atmospheres*, *118*, 416–434. https://doi.org/10.1029/2012JD018658

Jiang, Q., Doyle, J. D., Reinecke, A., Smith, R. B., & Eckermann, S. D. (2013). A modeling study of stratospheric waves over the southern Andes and Drake Passage. *Journal of the Atmospheric Sciences*, *70*(6), 1668–1689, https://doi.org/10.1175/JAS-D-12-0180.1

John, S. R., & Kumar, K. K. (2013). A discussion on the methods of extracting gravity wave perturbations from space-based measurements. *Geophysical Research Letters*, *40*, 2406–2410. https://doi.org/10.1002/grl.50451

Kaifler, B., Kaifler, N., Ehard, B., Dörnbrack, A., Rapp, M., & Fritts, D. C. (2015). Influences of source conditions on mountain wave penetration into the stratosphere and mesosphere. *Geophysical Research Letters*, *42*, 9488–9494. https://doi.org/10.1002/2015GL066465

Kaifler, B., Lübken, F.-J., Höffner, J., Morris, R. J., & Viehl, T. P. (2015). Lidar observations of gravity wave activity in the middle atmosphere over Davis (69°S, 78°E), Antarctica. *Journal of Geophysical Research: Atmospheres*, *120*, 4506–4521. https://doi.org/10.1002/2014JD022879

Kogure, M., Nakamura, T., Ejiri, M. K., Nishiyama, T., Tomikawa, Y., Tsutsumi, M., et al. (2017). Rayleigh/Raman lidar observations of gravity wave activity from 15 to 70 km altitude over Syowa (69°S, 40°E), the Antarctic. *Journal of Geophysical Research: Atmospheres*, *122*, 7869–7880. https://doi.org/10.1002/2016JD026360

Kursinski, E. R., Hajj, G. A., Schofield, J. T., & Linfiled, R. P. (1997). Observing Earth's atmosphere with radio occultation measurements using the Global Positioning System. *Journal of Geophysical Research*, *102*, 23,429–23,466. https://doi.org/10.1029/97JD01569

Lee, A. M., Roscoe, H. K., Jones, A. E., Haynes, P. H., Shuckburgh, E. F., Morrey, M. W., & Pumphrey, H. C. (2001). The impact of the mixing properties within the Antarctic stratospheric vortex on ozone loss in spring. *Journal of Geophysical Research*, *106*, 3203–3211. https://doi.org/10.1029/2000JD900398

Llamedo, P., Hierro, R., de la Torre, A., & Alexander, P. (2016). ENSO-related moisture and temperature anomalies over South America derived from GPS radio occultation profiles. *International Journal of Climatology*. https://doi.org/10.1002/joc.4702

Luna, D., Alexander, P., & de la Torre, A. (2013). Evaluation of uncertainty in gravity wave potential energy calculations through GPS radio occultation measurements. *Advances in Space Research*, *52*(5), 879–882. https://doi.org/10.1016/j.asr.2013.05.015

Luntama, J.-P., Kirchengast, G., Borsche, M., Foelsche, U., Steiner, A., & Healy, S. (2008). A. von Engeln, E. O'Clerigh, and C. Marquardt, Prospects of the EPS GRAS mission for operational atmospheric applications. *Bulletin of the American Meteorological Society*. https://doi.org/10.1175/2008BAMS2399.1

McGee, T. J., Gross, M., Ferrare, R., Heaps, W., & Singh, U. (1993). Raman dial measurements of stratospheric ozone in the presence of volcanic aerosols. *Geophysical Research Letters*, *20*, 955–958. https://doi.org/10.1029/93GL00751

McLandress, C., Shepherd, T. G., Polavarapu, S., & Beagley, S. R. (2012). Is missing orographic gravity wave drag near 60°S the cause of the stratospheric zonal wind biases in chemistry–climate models? *Journal of the Atmospheric Sciences*, *69*(3), 802–818. https://doi.org/10.1175/JAS-D-11-0159.1

Nappo, C. J. (2002). *An introduction to atmospheric gravity waves*, *International Geophysics Series*, (p. 279). San Diego, CA: Academic Press.

Nash, E. R., Newman, P. A., Rosenfield, J. E., & Schoeberl, M. R. (1996). An objective determination of the polar vortex using Ertel's potential vorticity. *Journal of Geophysical Research*, *101*, 9471–9478. https://doi.org/10.1029/96JD00066

Plougonven, R., Hertzog, A., & Guez, L. (2013). Gravity waves over Antarctica and the Southern Ocean: Consistent momentum fluxes in mesoscale simulations and stratospheric balloon observations. *Quarterly Journal of the Royal Meteorological Society*, *139*(670), 101–118. https://doi.org/10.1002/qj.1965

Plougonven, R., & Zhang, F. (2014). Internal gravity waves from atmospheric jets and fronts. *Reviews of Geophysics*, *52*, 33–76. https://doi.org/10.1002/2012RG000419

Preusse, P., Ern, M., Bechtold, P., Eckermann, S. D., Kalisch, S., Trinh, Q. T., & Riese, M. (2014). Characteristics of gravity waves resolved by ECMWF. *Atmospheric Chemistry and Physics*, *14*(19), 10,483–105,08, https://doi.org/10.5194/acp-14-10483-2014

Pulido, M., Rodas, C., Dechat, D., & Lucini, M. M. (2012). High gravity-wave activity observed in Patagonia, Southern America: Generation by a cyclone passage over the Andes mountain range. *Quarterly Journal of the Royal Meteorological Society*. https://doi.org/10.1002/qj.1983

Remsberg, E. E., Marshall, B. T., Garcia-Comas, M., Krueger, D., Lingenfelser, G., Martin-Torres, J., et al. (2008). Assessment of the quality of the version 1.07 temperature-versus-pressure profiles of the middle atmosphere from TIMED/SABER. *Journal of Geophysical Research*, *113*, D17101. https://doi.org/10.1029/2008JD010013

Richter, J. H., Sassi, F., & Garcia, R. R. (2010). Toward a physically based gravity wave source parameterization in a general circulation model. *Journal of the Atmospheric Sciences*, *67*(1), 136–156. https://doi.org/10.1175/2009JAS3112.1

Sato, K., Tateno, S., Watanabe, S., & Kawatani, Y. (2012). Gravity wave characteristics in the Southern Hemisphere revealed by a high resolution middle-atmosphere general circulation model. *Journal of the Atmospheric Sciences*, *69*(4), 1378–1396. https://doi.org/10.1175/JAS-D-11-0101.1

Schmidt, T., Alexander, P., & de la Torre, A. (2016). Stratospheric gravity wave momentum flux from radio occultations. *Journal of Geophysical Research: Atmospheres*, *121*, 4443–4467. https://doi.org/10.1002/2015JD024135

Schmidt, T., Wickert, J., Marquardt, C., Beyerle, G., Reigber, C., Galas, R., & König, R. (2004). GPS radio occultation with CHAMP: An innovative remote sensing method of the atmosphere. *Advances in Space Research*, *33*(7), 1036–1040.https://doi.org/10.1016/S0273-1177(03)00591-X

Shibata, T., Kobuchi, M., & Maeda, M. (1986). Measurements of density and temperature profiles in the middle atmosphere with a XeF lidar. *Applied Optics*, *25*(5), 685–688. https://doi.org/10.1364/AO.25.000685

Wolfram, E. A., Salvador, J., D'Elia, R., Casiccia, C., Paes Leme, N., Pazmiño, A., et al. (2008). New differential absorption lidar for stratospheric ozone monitoring in Patagonia, South Argentina. *J. Opt. A: Pure Appl. Opt.*, *10*(10), 104021. https://doi.org/10.1088/1464-4258/10/10/104021

Wolfram, E. A., Salvador, J., Orte, F., D'Elia, R., Godin-Beekmann, S., Kuttippurath, J., et al. (2012). The unusual persistence of an ozone hole over a southern mid-latitude station during the Antarctic spring 2009: A multi-instrument study. *Annales de Geophysique*, *30*(10), 1435–1449. https://doi.org/10.5194/angeo-301435-2012

Wright, C. J., Hindley, N. P., Hoffmann, L., Alexander, M. J., & Mitchell, N. J. (2017). Exploring gravity wave characteristics in 3-D using a novel S-transform technique: AIRS/Aqua measurements over the southern Andes and Drake Passage. *Atmospheric Chemistry and Physics*, *17*(13), 8553–8575. https://doi.org/10.5194/acp-17-8553-2017

Wright, C. J., Hindley, N. P., Moss, A. C., & Mitchell, N. J. (2016). Multiinstrument gravity-wave measurements over Tierra del Fuego and the Drake Passage—Part 1: Potential energies and vertical wavelengths from AIRS, COSMIC, HIRDLS, MLS-Aura, SAAMER, SABER and radiosondes. *Atmospheric Measurement Techniques*, *9*(3), 877–908, https://doi.org/10.5194/amt-9-877-2016

Zhang, F. (2004). Generation of mesoscale gravity waves in upper-tropospheric jet-front systems. *Journal of the Atmospheric Sciences*, *61*(4), 440–457.

Zhang, F., Koch, S., Davis, C., & Kaplan, M. (2000). A survey of unbalanced flow diagnostics and their application. *JAdvances in Atmospheric Sciences*, *17*(2), 165–183.